

AN X-RAY INTERFEROMETRIC OBSERVATORY

Christopher Martin

*California Institute of Technology'
Pasadena, California***Abstract**

X-ray interferometry has the potential for observations of unprecedented angular resolution and far-reaching astrophysical consequences. I present here a new concept for an x-ray interferometric observatory that obtains an angular resolution 10^5 times better than AXAF. Using a grazing incidence fringe spectrum design, the x-ray interferometer operates over a broad band (0.24 keV), with ~ 18 concentric Wolter-Schwarzschild mirror shells of diameter **0.6-2.4** meters. A fringe-sensitive detector measures the amplitude and phase of closely spaced Fizeau fringes in the focal plane. Fringe phasing is maintained using an optical metrology system and two optical Michelson stellar interferometers to provide absolute inertial reference for the phase tracking center. Mirror phasing is maintained with active control of low spatial frequency figure errors. The interferometer furnishes high spectral resolution ($E/\Delta E > 10^4$), and realizes high sensitivity by minimizing the number of optical components and by operating over a broad band. The interferometer is capable of obtaining detailed spectrally resolved images of stellar coronae, broad-line regions and jets of many AGNs, and the accretion disks of a selection of bright AGNs and QSOs.

I. Introduction and Motivation

It is almost (but not quite) taken for granted by most astrophysicists that large enhancements in observational capability are returned with a generous dividend of both predictable and surprising results. However, as the complexity and cost of these efforts grows, their scientific justification must be keen enough to drive them forward against the innumerable technical and political challenges. Observational leaps come in four general directions: exploration of new bands of the electromagnetic spectrum and new forms of radiation, improvements in light-gathering power and time resolution, enhancements in spectroscopy, and augmentations in imaging capability. In the x-ray band, improvements in imaging have lagged behind those in the optical, infrared, and radio, for well-known technical and historical reasons. While ultra-high resolution imaging is being aggressively pursued from the radio to the UV, its potential for x-ray astrophysics is only beginning to be explored (e.g., Cash 1990 and Martin 1990).

High resolution x-ray imaging will be pursued only if (1) it promises an extraordinary scientific return; (2) a powerful and practical design concept is developed and its feasibility demonstrated; and (3) the effort is part of a broad international program for ground- and space-based high resolution imaging and astrometry.

There are a number of powerful, general arguments for pursuing x-ray interferometry. At x-ray wavelengths, it is possible to obtain the highest angular resolution with modest baselines. An x-ray interferometer with the same diameter as Hubble Space Telescope has resolution 10^4 times

*Much of this paper was written while at Columbia University, New York, New York

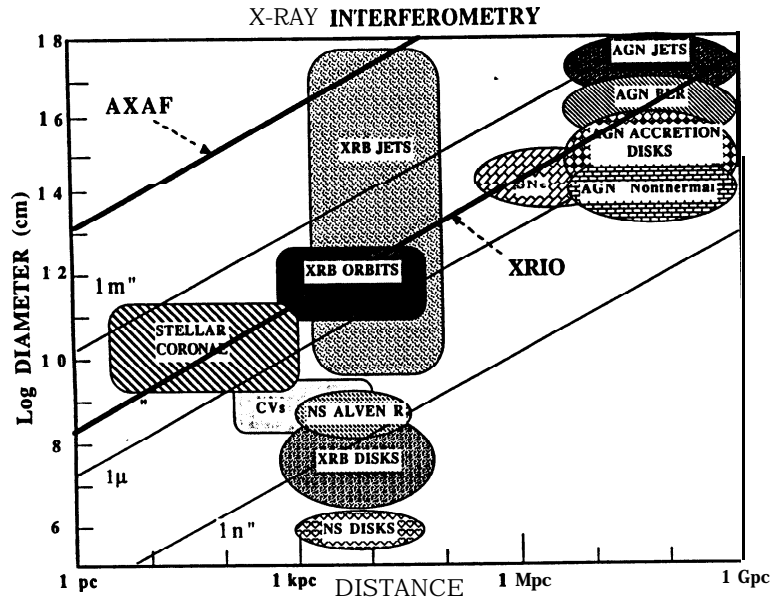


Figure 1: Angular diameter of various x-ray sources.

greater. Many x-ray sources are compact, with high surface brightness and small angular size. They can be imaged at high resolution with moderate apertures. The structure and energetics of compact x-ray sources, x-ray binaries, AGNs, as well as stellar coronae, are fundamentally mysterious. X-ray interferometry will represent a leading partner in multiwavelength interferometric mapping of these objects. Looking ahead, x-ray interferometry offers the only chance for imaging neutron star surfaces and black hole horizons.

A preliminary road map to the scientific potential of high resolution x-ray imaging is provided in Figure 1, which gives the typical angular sizes of a variety of x-ray emitters. Imaging of nearby stellar coronae and active galactic nuclei (AGN) inner jets requires 0.01- 1 milliarcsecond resolution. Resolving AGN accretion disks, jets in x-ray binaries, and the measurement of x-ray binary orbital parameters require resolution in the 0.1- 100 μ'' range. Imaging of neutron star disks and accretion disks in x-ray binaries will only be possible with nanoarcsecond resolution.

This graph illustrates a fundamental constraint: we will derive the maximum benefits from and justification for high resolution x-ray imaging if our goal is resolution in the 10-1000 microarcsecond range. The design concept presented in this paper exploits x-ray interferometry to obtain 10-1000 μ'' resolution. In the following few paragraphs, I highlight some of the scientific motivation for x-ray imaging at this resolution.

Stellar Coronae. The dynamo mechanism in stars, and the heating of stellar coronae are two unsolved mysteries of stellar astrophysics. X-ray imaging of extrasolar coronae would provide critical information on the emission volume, distribution, magnetic field configuration, relationship to rotation rate and companions in binary systems, and the time variability of these conditions. There are many important questions: How does the size and distribution of magnetic loops scale with stellar type, age, and rotation rate? What is the temperature structure in the loops? What is the magnetic field configuration in active close binaries, and how does the dynamo mechanism vary in these systems? Imaging O-stars would provide critical information about the perplexing question of the source of x-rays in these systems.

X-ray Binaries and X-ray Astrometry. We could search for extended emission in x-ray binaries produced by jets. Some accretion disks may have extended coronae that could be resolved. The brightness of galactic x-ray sources and the extensive *uv-plane* coverage of the proposed interferometer make possible high-dynamic range imaging of x-rays reflected from the accretion disk, accretion flow, and secondary companion star. With astrometric capability that can in principle be incorporated in an interferometric observatory, it would be possible to trace the orbit of the x-ray source in a binary system relative to that of the optical companion, and make an unambiguous determination of the orbital elements and stellar masses. This would provide a definitive test of the black hole hypothesis in several x-ray binaries.

Supernovae. Supernovae such as 1980k and 1987a produced copious soft x-ray emission at some time in their early life. Imaging these x-rays would provide direct information about the mechanism producing them, while probing the isotropy of the supernova blast wave, the surrounding relic stellar wind, and the nature of the progenitor star.

Active Galactic Nuclei. With sub-milliarcsecond resolution, we could search for x-ray jets and evidence for interactions of relativistic particles and the ambient medium around the AGN. We could determine the contribution of jet emission to the total x-ray luminosity. X-ray emission from jets is presumably a result of thermal gas produced by shocks, inverse Compton scattering of optical nuclear radiation or synchrotron emission from extremely relativistic electrons. Spectrally-resolved imaging of x-ray emission from jets very near the central engine could help solve a long-standing puzzle: the physical mechanisms of jet formation and collimation. It should be possible to resolve and map any hot gas intercloud gas in the broad line regions of AGNs. The statistical absorption of broadline clouds may even be detectable, providing a map of the broad line cloud geometry, a critical missing element in the interpretation of optical emission lines. The prospect of actually imaging an accretion disk around a massive black hole stands as unprecedented experimental challenge with a fantastic payoff. Resolution of an accretion disk would stand as a definitive proof of the massive black hole/accretion disk paradigm for AGNs. The aspect ratio would give the disk thickness and inclination, the position angle the orientation on the sky and relative to radio and optical features such as jets and the galactic disk. It would be extremely interesting to relate the accretion disk and jet morphology to the x-ray variability. At higher energies, there is fundamental uncertainty about the mechanisms producing the non-thermal continuum. In 3C273 and several other AGNs with bright Fe K lines, it may be possible to perform spatially-resolved spectroscopy of the Fe K and L-shell fluorescence from the accretion disk.

How can x-ray imaging with 10-100 μ'' resolution be achieved? An x-ray telescope with a filled aperture of 2.4 m diameter, operating at Fe K 6.4 keV, would in fact obtain 16 μ'' resolution. However, the numerous grazing incidence mirror shells would have to be figured and phased together to within a fraction of an Angstrom. Even more serious is the difficulty in resolving the resulting image. Using a detector with 1 μm resolution, an effective focal length of 20 km would be required! An x-ray microscope at the focus of a more practical telescope could help, but the resolution and magnification requirements are impossible to obtain in a grazing incidence microscope. A normal incidence multilayer microscope has the potential to obtain exquisite x-ray images of the sun (e.g., Shealy *et al.* 1989), but the limited bandpass and low overall efficiency would severely limit the power of the telescope for stellar and extragalactic astronomy.

Broadband x-ray interferometry offers a solution to these difficulties. Unfilled aperture interferometry is being vigorously pursued and discussed from the submillimeter band through the ultraviolet. X-ray interferometry has not been discussed, because of the technical difficulties that it will entail, and because a workable concept has not been proposed. However, many of the necessary technologies are also required for the Astrometric Interferometry Mission (AIM), which is being vigorously studied by NASA and JPL for a new start near the turn of the century. Some of the con-

ceptual foundations for the design outlined in this paper can be found in the nonredundant masking technique used for ground-based optical interferometry (e.g., Kulkarni 1988).

Astronomical x-ray interferometry has as a foundation a surprisingly extensive history of laboratory demonstration and application. The first experiment to produce x-ray interference fringes was undertaken 60 years ago. Kellström (1932) used a Lloyd's mirror arrangement to demonstrate x-ray interference at $\lambda = 8\text{\AA}$. Nearly thirty years ago, Bonse and Hart (1965) produced the first Bragg crystal interferometer operating at $\lambda = 1.54\text{\AA}$. X-ray interferometry has been used to measure indices of refraction (Rocket 1985), for precision metrology (Becker *et al.* 1987), and to determine x-ray to visible wavelength ratios (Deslattes and Henins 1973). Martin (1990) has discussed an astronomical x-ray interferometer using a lunar-based multilayer mirrors and pupil-plane fringe detection in a Michelson interferometer, for $\lambda \sim 44\text{\AA}$.

The design presented in this paper is a significant improvement over the lunar-based concept in four crucial areas: it covers a broad band (0.2-8 keV); it uses a monolithic x-ray telescope and detector; it furnishes true imaging with sensitivity sufficient to exploit the resulting high angular resolution; finally, it exploits technology for space-based interferometry that is being actively pursued for the Astrometric Interferometry Mission. In section II, I discuss the general requirements for an x-ray interferometer. Then in section III, I outline in some detail a concept for a broadband x-ray interferometer that obtains $\sim 10\ \mu''$ angular resolution, spectral resolution $E/\Delta E > 10^3$, and high sensitivity. The paper is summarized in section IV, with an eye toward future developments that must be pursued to realize an x-ray interferometric observatory.

II. Design Guidelines

This section summarizes the basic requirements for an astronomical x-ray interferometer. In dilute aperture interferometry, separate portions of the x-ray wavefront are made to overlap and interfere coherently. For simplicity we restrict our attention to systems with two overlapping beams. Assuming the source is not resolved, and the path lengths of the two beams are equal to within a coherence length, x-ray fringes are formed which must be measured either in the pupil plane or in the focal plane. The fringe amplitude is related to the amplitude of the complex visibility function for the source $V(u, v)$, where u and v are as usual the baseline components measured in wavelengths. The phase of the fringes relative to a fixed reference gives the phase of $V(u, v)$.

1. Path length equalization:

Coherent interference between two widely separated wavefront samples occurs only when the path lengths are equal to within a coherence length $l_c \simeq \lambda^2/\Delta\lambda$, where $\Delta\lambda$ is the bandwidth at detection. For $\lambda = 0.5\text{ nm}$ and $\lambda/\Delta\lambda = 10^4$, the coherence length $l_c = 5\ \mu\text{m}$. In the x-ray band, reflections must be minimized for reasons of efficiency, and normal incidence reflections cannot be exploited to permit path-length compensation. Symmetry of the two optical paths is essential, and the use of sidereostats limited or impossible. Active control of the optical paths may be necessary.

2. Full-aperture phasing to $\sim 0.1\lambda_x$:

A most formidable challenge in the construction of an x-ray interferometer is phasing two interfering wavefronts to within a fraction of a wavelength, over the full baseline and aperture. As long as the optical path lengths are kept equal to within the coherence length, the relative path lengths only need to be monitored, but not controlled, to $\sim 0.1\lambda_x$. This requires an accurate knowledge of path length errors developed in the instrument, and of those introduced by errors and drifts in the

source tracking relative to the instrument. The former requires a metrology system that can measure and track path length errors over the full aperture, or over enough points that interpolation is accurate. At an x-ray wavelength of 0.5 nm, optical path metrology is required to $\sim 0.02\text{-}0.05$ nm, or 1 part in 10^{11} of a 2 m baseline. Metrology at this level is within the capabilities of fringe scanning Michelson and Fabry-Perot type interferometers operating at visible wavelengths. This has been demonstrated by the application of interferometric techniques for gravity wave “beam detectors”. The ultimate goal of beam detectors is to measure a gravity wave induced strain of $< 10^{-20}$ over tens of kilometers, a task that is *ten million* times more demanding than required for x-ray interferometry.

Source tracking is also a critical problem for maintaining phasing. Stability is required to $\Delta\theta_s < l_c/B$ with knowledge to $\Delta\theta_k < 0.1\lambda/B$ radians. For the observatory proposed below, a tracking knowledge of $2\mu''$ is required. This could be provided by a pair of optical interferometers deployed with their baselines parallel to the x-ray telescope axis, observing two bright stars at roughly 90 degrees to each other and the x-ray source. The relatively coarse roll axis could be stabilized with a smaller high precision star tracker.

3. Beam overlap and Fringe Formation:

The beams must be made to overlap, coherently and in such a way that the resulting interference fringes are detectable. Systems with baselines less than a few meters can use grazing incidence optics, as will be shown below. The length of a grazing incidence interferometer is $L_{int} \sim 15B/\gamma N_r$, where γ is the graze angle in degrees and N_r is the number of reflections prior to combination. A long-baseline lunar based interferometer (Martin 1990) requires sidereostats, which can only be made using large angle reflections furnished by multilayer mirrors operating at long wavelengths.

Interference fringes are formed when two beams from separate parts of the wavefront are permitted to overlap. Fringes may be observed in either the focal plane (Fizeau 1868) or the pupil plane (pupil plane fringes). Michelson’s stellar interferometer used Fizeau fringes (Michelson 1920). The spacing of Fizeau fringes is $\Delta x(nm) = \lambda(nm)(F/B)$, and is generally quite small. For x-ray telescopes with two reflections, $10 < F/B < 50$. For example, for $F=30$ m, $B=1.5$ m, and $\lambda = 0.5$ nm, the fringe spacing is 10 nm. In spite of these microscopic dimensions, x-ray Fizeau fringes may be measurable with a suitable detector (see below).

Pupil plane fringes can only be formed by causing the pupils from widely separated portions of the wavefront to overlap. This can only be accomplished using a beam splitter. X-ray beam splitters could be furnished by gratings (Rocket 1985), Bragg Crystals (Bonse and Hart 1965), multilayer mirrors (Lee 1982), or semitransparent reflectors (Martin 1990). These techniques are invariably limited in bandwidth to $\Delta E/E < 0.1$.

4. Fringe detection:

With an unresolved source, constructive interference occurs when the two optical paths are equal modulo one wavelength. Variation of the relative optical path of one beam by $\lambda/2$ produces destructive interference. When the relative path length varies by one wavelength, the amplitude of the complex visibility function can be determined from the variation in received intensity in the fringe detector at one baseline.

Visibility is often most easily measured in the pupil plane (Shao *et al.* 1988). Path length errors produced by a variety of influences result in fringes in the pupil plane. As the relative optical paths are varied over a wavelength, the fringes will become alternately light and dark (with an amplitude contrast determined by the visibility). Imaging these fringes in the pupil plane allows increased tolerance to these path length errors.

Visibility measurement using focal plane Fizeau fringes, while more challenging, may provide the only alternative to the narrow band performance of all x-ray beam splitters. Measurement of Fizeau fringes can only be accomplished by a detector filter combination sensitive to ultra-high spatial frequencies. The spatial resolution of any x-ray detector is limited by the size of the secondary electron cloud created following the ejection of a primary photoelectron. This cloud has a diameter $D_{ec}(nm) = 17E^{1.75}$ in Si (Bresse 1972). If the centroid of the secondary electron cloud could be measured, the fundamental limit to the resolution (in Si) is $\sigma_{ec}(nm) = 1 E^{1.25}$. A fano-limited CCD with $\sim 1 \mu m$ pixels with a diffusion region that allowed the cloud to expand into several adjacent pixels could determine a cloud centroid to < 100 nm. This is not adequate to resolve fringes at the smallest spacings required for a practical interferometer. A Gaussian detector blur degrades the visibility by a factor

$$V_{det} = e^{-(2\pi\sigma/\Delta p)^2}, \quad (1)$$

where σ is the detector rms resolution and Δp is the fringe period. With $\sigma/\Delta p=0.5$, the detector “visibility” is reduced to 0.76. Thus the direct position determination in a detector cannot be exploited to measure fringe spacings smaller than ~ 10 nm. For x-ray interferometers with practical focal lengths and baselines, this limits the ultimate angular resolution seriously. However, one can contemplate an x-ray detector that would be sensitive to a *periodic* high spatial frequency signal. The idea is to fabricate a laminar structure, with alternating high and low absorption efficiency material, having a lamination period equal to the fringe spacing. The structure could be used either as a filter, or as the detecting structure itself. The details of this technique are discussed below.

III. A Broad-band X-ray Interferometric Observatory

A. Concept Summary

An x-ray interferometric observatory can be constructed which delivers (1) angular resolution promising major astrophysical insight ($\sim 10 \mu''$); (2) good sensitivity sufficient to exploit that resolution; (3) broadband coverage, from the C K (4.4 nm) through Fe K (0.15 nm) ; and (4) simultaneous high resolution spectroscopy. The concept and preliminary design, presented below, utilize techniques which will or can be developed in the next 10-20 years.

The observatory is shown schematically in Figure 2. A Wolter-Schwarzschild (WS) telescope consisting of 18 mirror shells is employed. The shells range in diameter from 0.6 m to 2.4 m, and the telescope focal length is $F = 30m$. Each shell is subdivided into ~ 8 *subaperture pairs* consisting of symmetrically placed rectangular openings. Assuming proper conditions are met, a rectilinear fringe pattern is formed by each pair at the focus of the detector when the telescope is illuminated by monochromatic light from a point source at infinity. The fringe visibility amplitude is identical to the visibility used in radio interferometry, where $|\tilde{V}(u, v)| = |V(\mathbf{B}/\lambda)|$. The phase of the complex visibility is given by the fringe phase measured against a fixed (inertial) reference. To provide for broadband fringe detection, light from each aperture pair is intercepted by transmission gratings following the mirrors. The gratings produce an x-ray fringe spectrum, yielding radial fringes with the distance from the telescope axis proportional to the wavelength. Each aperture pair/grating combination gives two fringe spectra extending perpendicular to the telescope axis and line joining the apertures. The fringe spectra produced by the 8×18 aperture pairs are accommodated on a single detector by arranging the lines joining the aperture pairs at slightly different azimuthal angles. The visibility amplitude and phase of the closely spaced fringes formed at the telescope focus are detected using an x-ray spatial heterodyne detector. Each aperture pair provides a different baseline, and the broadband sensitivity gives a well sampled uv [image Fourier transform] plane to $u_{max} \simeq 10^{10}$. Approximately two-thirds of the telescope aperture is devoted to interferometry. The

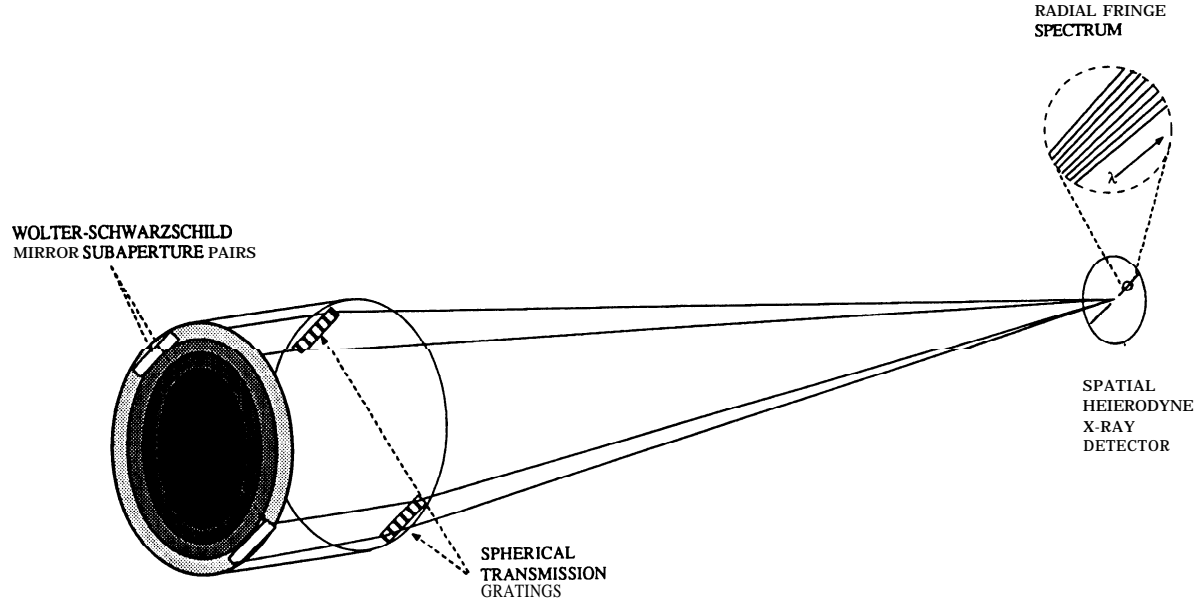


Figure 2: Schematic of broadband X-ray interferometric observatory. Figure shows a single sub-aperture pair.

remaining fraction is used for imaging spectroscopy with an angular resolution of $\sim 1\text{m}''$. The observatory obtains a sensitivity comparable to the AXAF CCD instrument, while obtaining spatially resolved spectroscopy with $\Delta\theta = 12\ \mu''$ and $\lambda/\Delta\lambda > 10^3$.

B. Fringe Formation in Paired Wolter-Schwarzschild Subapertures

A single azimuthal section of an imperfect WS mirror will produce an image that is elongated in the plane of incidence, since surface errors on the mirror are projected to high spatial frequency in the plane of incidence, by a factor $\csc(\gamma)$. This property can be exploited for high resolution imaging in one dimension (Cash 1990). Placement of a second azimuthal section opposite the first will generate interference fringes, if the telescope is illuminated by collimated, monochromatic light. I call this a *subaperture pair*. These have spacing $(F/B)\lambda$, where F is the focal length and \mathbf{B} is the separation (or baseline) vector between the two sections. For grazing incidence telescopes, F/B is typically in the range of 10-50.

If the mirrors are perfect, then the fringe pattern is simply the two slit pattern modulated by the subaperture diffraction pattern. In this case, the fringe *visibility*, defined as

$$V = \frac{I_{\max} - I_{\min}}{I_{\max} + I_{\min}}, \quad (2)$$

is unity. The intensity distribution has been integrated along the direction perpendicular to \mathbf{B} . When the mirrors are imperfect in figure, or introduce aberrations, fringe visibility is reduced.

We can determine these effects if the wavefront error function $\Delta(\xi, \eta)$ is known. Here, A measures the deviation of the final wavefront from a perfect sphere converging on the telescope focus. It is given in terms of the aperture coordinates ξ and η , where the baseline is along the t -axis. The focal-plane fringe intensity pattern can be calculated using simple Fraunhofer-Kirchhoff scalar

diffraction theory, in which the intensity function $I(p, q)$ is

$$I(\mathbf{p}) = \left| \int \int e^{ik\mathbf{p} \cdot \boldsymbol{\xi}} e^{ik\Delta(\boldsymbol{\xi})} A(\boldsymbol{\xi}) d\xi d\eta \right|^2. \quad (3)$$

We have assumed a monochromatic point source at infinity. The aperture function, $A(\boldsymbol{\xi})$ is unity in two rectangles centered at $\boldsymbol{\xi} = (-B/2, 0)$ and $\boldsymbol{\xi} = (+B/2, 0)$, with widths $\Delta\xi$ and $\Delta\eta$, and zero everywhere else. An annular aperture would produce curved fringes, which is undesirable for reasons outlined in the next section. The focal plane position, expressed in radians, is $\mathbf{p} = (p, q)$, with the p component in the plane of incidence (and parallel to \mathbf{B}). Refer to Figure 7 for the coordinate definitions used throughout this paper.

We can calculate the fringe visibility by integrating the intensity distribution directly against $\exp(ik\mathbf{p} \cdot \mathbf{B})$,

$$V_{mir}(\mathbf{B}/\lambda) = \frac{\int I(p, q) e^{ik\mathbf{p} \cdot \mathbf{B}} dq dp}{\int I(p, q) dq dp}. \quad (4)$$

The resulting visibility is complex, with the amplitude giving the fringe amplitude as defined in (2), and the phase giving the fringe phase. The result is remarkably simple. We define a new function

$$\Delta_1(x, y) = \Delta(x + B/2, y) - \Delta(x - B/2, y), \quad (5)$$

nonzero over $(-\Delta\xi/2 < x < \Delta\xi/2)$ and $(-\Delta\eta/2 < y < \Delta\eta/2)$, which gives the difference in the wavefront errors between equivalent points on the two apertures. Then, it can be shown that the visibility is exactly

$$V_{mir}(\mathbf{B}/\lambda) = \langle e^{ik\Delta_1} \rangle. \quad (6)$$

Here, the average is defined as

$$\langle f(x, y) \rangle = \frac{1}{\Delta\xi \Delta\eta} \int_{-\Delta\xi/2}^{+\Delta\xi/2} \int_{-\Delta\eta/2}^{+\Delta\eta/2} f(x, y) dx dy. \quad (8)$$

Thus, when $k\Delta_1 > 1$ and varies rapidly across the aperture, the visibility is close to zero. When $k\Delta_1 < 1$, we can expand the exponential and write the visibility as:

$$V_{mir} \simeq 1 - k^2 \langle \Delta_1^2 \rangle - ik \langle \Delta_1 \rangle \quad (7)$$

The visibility amplitude is then

$$|V_{mir}| \simeq 1 - k^2 [\langle \Delta_1^2 \rangle - \langle \Delta_1 \rangle^2] \quad (9)$$

while the fringe phase is

$$\tan \phi = \frac{-k \langle \Delta_1 \rangle}{1 - k^2 \langle \Delta_1^2 \rangle}. \quad (10)$$

For a grazing incidence telescope, this gives a corresponding requirement for the figure of each mirror:

$$\delta_{rms} < \frac{\lambda}{8\pi\gamma} \sqrt{1 - V_{mir}}. \quad (10)$$

Here, δ_{rms} is the rms deviation of the mirror figure from perfection, measured in the direction normal to the surface. We used the fact that reflection gives a factor of two more error, grazing incidence reduces the amplitude of mirror figure errors by $\sin \gamma$, and the combination of two mirrors

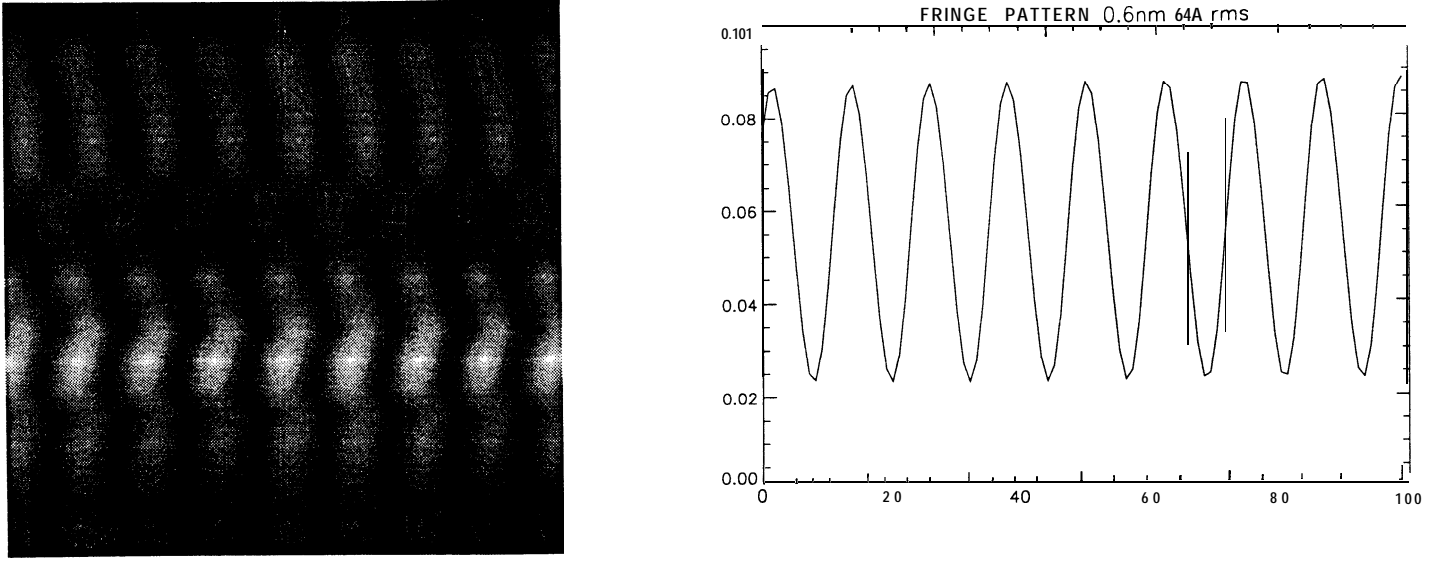


Figure 3: Simulations of interference fringes formed by Wolter-Schwarzschild subaperture pairs, and assuming AXAF goal surface figure errors with variable normalization. LEFT is 2-D fringe pattern, RIGHT is 1-D fringe visibility, and $\lambda=0.6$ nm, and $\delta_{rms}=64\text{\AA}$ rms.

increases the error by $\sqrt{2}$. I also assumed that the figure errors in the two apertures are completely uncorrelated. In practice, some correlation will be present which will increase the fringe visibility. For example, axial figure errors that are azimuthally symmetric will be completely correlated! It should also be pointed out that the average is taken over a small subset of the entire mirror surface. In any event, to achieve a visibility $V_{mir} > 0.8$, for $\lambda=1$ nm, and a graze angle of 10 mrad, the uncorrelated figure errors must have $\delta_{rms} < 20\text{\AA}$ rms for each mirror, or roughly eight times better than the AXAF specification for all errors.

The detailed effect of mirror imperfections depends on the autocovariance function of the mirror surface. To investigate this, the two dimensional distribution of fringes in the focal plane was calculated exactly, using the AXAF mirror autocovariance function specification (*goal*; Van Speybroeck *et al.* 1989). The acf was scaled by a total rms error δ_{rms} , which was varied. The intensity distribution was calculated using the simple Fraunhofer-Kirchhoff scalar diffraction theory of equation (3). Some examples of the simulation are illustrated in Figure 3. The one dimensional distributions $I(p) = \int I(p, q) dq$ are also given. When δ_{rms} is small, the fringes are straight with high visibility. As δ_{rms} grows, the fringes become distorted, which reduces the visibility in the 1-D distribution $I(p)$. Figure 4 summarizes the dependence of fringe visibility on δ_{rms} for various wavelengths. In order to maximize the sensitivity to fringe visibility up to the Fe K line, the mirrors must have figures good to $\sim 4\text{\AA}$ rms, roughly a factor of 40 better than the AXAF mirror specification goal. I will discuss in section III.F how this might be achieved in practice.

When the mirror pair is illuminated by an extended source, with angular distribution $S(\mathbf{p})$, the resulting focal plane intensity distribution is a convolution of the point source fringe pattern $I(\mathbf{p})$ and the source distribution: $I'(\mathbf{p}) = I * S$. Then, from the convolution theorem, the Fourier transform performed in equation (4) yields the product of the mirror visibility function and the source visibility function:

$$V_{obs}(\mathbf{B}/\lambda) = V(\mathbf{B}/\lambda) V_{mir}(\mathbf{B}/\lambda). \quad (12)$$

Here, $V(\mathbf{B}/\lambda)$ is the 2-D Fourier transform of the source distribution at the (u, v) -plane point \mathbf{B}/λ

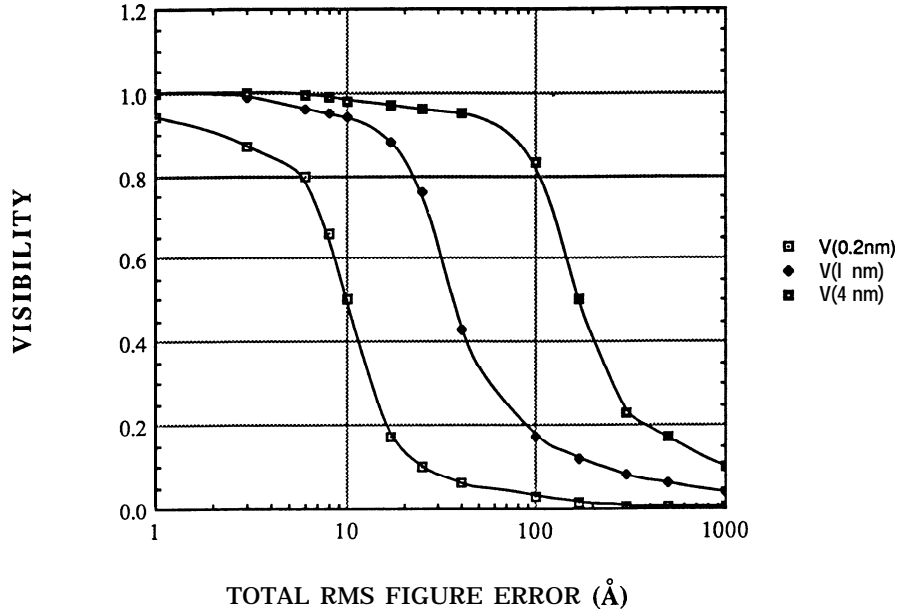


Figure 4: Summary of fringe visibility vs. mirror figure error, for three different wavelengths, based on simulations using AXAF surface error specification.

(relative to the phase tracking center), identical to the complex visibility as used in radio astronomy. Thus the complex visibility of the source can be recovered only if the mirror visibility function $V_{mir} = \langle e^{ik\Delta_1} \rangle$ (both phase and amplitude) at each baseline and wavelength is known. An optical system for measuring Δ_1 as well as detector-related visibility errors is discussed in section III.F.

C. Broad-Band Interference Fringes

For reasons of sensitivity, spectral coverage, alignment and tracking control tolerance, it is extremely desirable to detect fringes over the entire soft x-ray band. The fringe visibility is reduced, however, as the bandwidth is broadened. Assume that the mirror image has a length \mathbf{Ap} in the plane of incidence, and a width \mathbf{Aq} in the perpendicular direction (both in radians). Then, roughly $\Delta p B / \lambda$ fringes would be formed. Visibility would be seriously degraded unless the bandwidth is limited to $\Delta \lambda / \lambda < \frac{\lambda}{\Delta p B}$. For $\mathbf{Ap} = 0.5 \mu\text{rad}$, and at 0.2 nm, $\Delta \lambda / \lambda < 2 \times 10^{-4}$! This is a prohibitively small bandwidth, into which few photons will ever arrive.

The solution is to disperse the fringes in such a way as to maintain local coherence of the interfering beams. This can be done by diffracting the beams from the two subapertures in the direction perpendicular to the baseline vector \mathbf{B} . Spherical transmission gratings affect this, on the Rowland circle intercepting the converging light from the WS mirror pair. Their grooves run parallel to \mathbf{B} . This geometry maintains symmetric optical paths, required to maintain coherence. It yields fringes that diverge radially from the telescope axis which now is the zero-order focus. This is illustrated schematically in Figure 5. Each subaperture-grating pair produces two first-order spectra on opposite sides of the zero order mirror focus. Figure 6 shows broadband radial fringes produced at optical wavelengths. Coordinate definitions are summarized in Figure 7.

The coherence limit is now influenced by the width of the image in the dispersion direction \mathbf{Aq} .

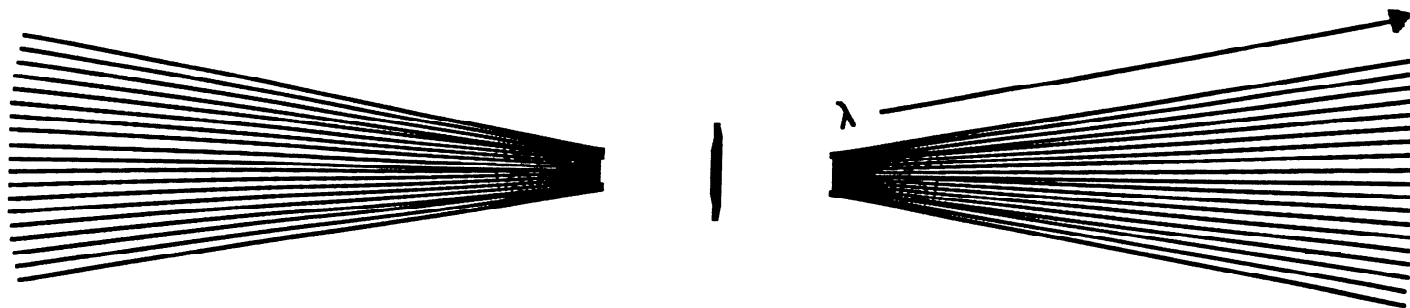


Figure 5: Radial interference fringes produced by interference of WS subaperture beams dispersed by spherical gratings.

Figure 6: Broad band radial interference fringes produced at optical wavelengths, using 19th-century lecture demonstration equipment.

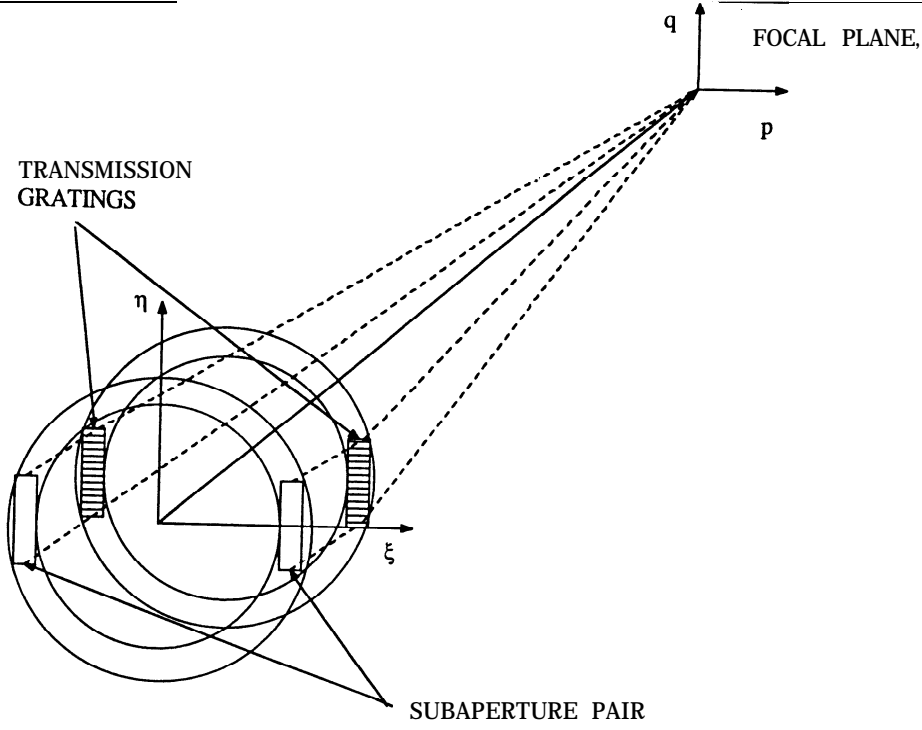


Figure 7: Orientation of Wolter mirror subapertures and transmission gratings, with coordinate systems used in this paper.

The width of the image perpendicular to the dispersion, Δp , also enters because it determines the average fringe tilt. We assume that the fringe envelope is a Gaussian with FWHM of Aq and Δp . This leads to a lower limit on the grating ruling frequency and angular dispersion:

$$\frac{1}{d} \geq 1.1 \frac{V}{\sqrt{1-V^2}} \frac{\Delta p \Delta q B}{\lambda^2}. \quad (13)$$

For an example, we allow $V = 0.95$, and $B = 2.4$ m, $A_p = 0.5 \mu\text{rad}$ ($100 m''$), $A_q = 0.005 \mu\text{rad}$ ($1 m''$), and $\lambda = 0.2$ nm. This gives a line density $1/d = 500$ l/mm. Note that the short-X limit determines the line density, while the long-X range fixes the length of the fringe spectra. The spectral resolution obtained by the optics is $x/\Delta x = (3.3B\Delta p/\lambda_{min})(\lambda/\lambda_{min})$. For the above parameter choices, $x/\Delta x = 10^5 \lambda(\text{nm})$. Whether or not this can be fully utilized depends on the detector resolution.

Grating aberrations have a negligible affect on the above conclusions. The important aberrations are astigmatism and coma (Schroeder 1987). These remain small because the dispersion angle β is small, even at the longest wavelengths, and because the subaperture beams are very slow, with focal ratios of $f_\xi \sim 1000$ and $f_\eta \sim 100$. With $\lambda_{max} = 5.0$ nm, $\beta_{max} = 8$ mrad. Astigmatism has no effect on the fringe visibility because the wavefront error is symmetric in ξ . Light from both apertures suffer the same path errors. Astigmatism could broaden the image in the p -direction, but this effect is negligible, since $AAS \sim \Delta\xi/F\beta_{max}^2 \simeq 3 \times 10^{-8}$ rad. Comatic wavefront error is also symmetric in ξ , since the spectrum is dispersed in the q -direction. Thus third order coma does not affect the fringe visibility either. Sagittal coma is too small to broaden the image width in the p -direction, since $ASC \sim 0.5(\Delta\xi/F)^2\beta_{max}^3 \sim 2 \times 10^{-13}$ rad. Tangential coma would blur the image in the q -direction, with $ATC \sim 0.125(\Delta\eta/F)^2\beta_{max}^3 \sim 6 \times 10^{-12}$ rad, still small compared to mirror blur. These conclusions can be demonstrated by consideration of equations (6) and (8). These conclusions were verified using the numerical model introduced above. The fringe patterns shown in Figure 3 included the transmission gratings, which had no effect on the visibility.

Transmission gratings are limited in efficiency to about 15-20% for both first orders. It may

be advantageous to use reflection gratings, which may achieve a factor of two to three increase in reflectivity. For this system, the gratings would be mounted in conical diffraction. While subject to more aberrations, many will cancel in this system, and many others may be diminished using varied-line space designs (Hettrick and Bowyer 1983; Cash 1983). A detailed consideration of this possibility is left to a future paper (Martin 1992).

D. Spatial Heterodyne X-ray Detectors

When the intensity distribution falling on the detector is periodic, with known period, it is possible to determine the amplitude and phase of the modulation without localizing each photon event to a fraction of a fringe width. What is required is a detector whose efficiency is periodically modulated at the known spatial frequency of the signal, a fact demonstrated by equation (4). This could be done two ways: (1) a periodic filter preceding the detector, or (2) a detector with periodic absorption efficiency. In both cases, this could be furnished by a laminar structure of alternating high Z /high ρ and low Z /low ρ material.

For example, a modulating filter could be constructed with alternating Mo/Si or W/C layers. Detector efficiency could be modulated by alternating layers of Si and SiO₂, Si and GaAs, or Si and Ge in the active absorption region. Visibility would be measured by moving the detector relative to the fringe pattern through at least one period, and observing the resulting modulation in countrate. Visibility phase would be determined by referring the position of maximum countrate to a phase reference. In this way the spatial heterodyne detectors demodulate the x-ray fringe pattern to dc.

The fringe pattern formed in the focal plane is in fact a standing wave pattern of nodal and antinodal planes parallel to the telescope axis, when considered in three dimensions. The fringe pattern extends over an axial distance $\sim F\Delta p/\sin 4\gamma$, since to a first approximation the two interfering beams can be considered to made of locally planar waves crossing at an angle 8γ . Thus the fringe pattern may have depth of $> 100 \mu\text{m}$. This is important because at higher energy, absorption depths reach $10 \mu\text{m}$. The operation of the spatial heterodyne detector is illustrated in Figure 8.

The modulation produced by such a detector can be calculated using a simple model. The two materials have linear absorption coefficients μ_1 and μ_2 , and the detector is t thick in the axial direction. The absorption efficiency in the two layers is $\epsilon_1 = 1 - e^{-\mu_1 t}$ and $\epsilon_2 = 1 - e^{-\mu_2 t}$. [For a transmission laminate, $\epsilon \rightarrow e^{-\mu t}$.] A fringe pattern following a $[1 + V \cos(kpB)]$ intensity profile gives a maximum and minimum countrates $R_{max} = 0.82\epsilon_1 - 0.18\epsilon_2$ and $R_{min} = 0.81\epsilon_1 - 0.82\epsilon_2$, where $\epsilon_1 > \epsilon_2$. In this case, the measured modulation in the detector $M = (R_{max} - R_{min}) / (R_{max} + R_{min})$ is

$$M = \frac{2}{\pi} \left(\frac{\epsilon_1 - \epsilon_2}{\epsilon_1 + \epsilon_2} \right) V \quad (14)$$

where V is the visibility of the fringes striking the detector. Clearly the optimal thickness t will increase slowly with energy. This variation can be built into the detector to match the grating dispersion.

Using equation (14), we can calculate the number of photons required to measure the fringe visibility to a given accuracy. The rms error in visibility σ_V due to photon statistics is

$$\sigma_V = \frac{\pi C_1}{2\sqrt{n_0}} \frac{\sqrt{\epsilon_1 + \epsilon_2}}{\epsilon_1 - \epsilon_2} \quad (15)$$

where n_0 is the number of photons arriving at the detector in one half of the total integration time T . The factor $C_0 = \int_0^1 4[0.7\epsilon_1\epsilon_2 + 0.15(\epsilon_1^2 + \epsilon_2^2)]/(\epsilon_1 + \epsilon_2)^2 \simeq 1$. The noise function $\sqrt{n_0}\sigma_V$

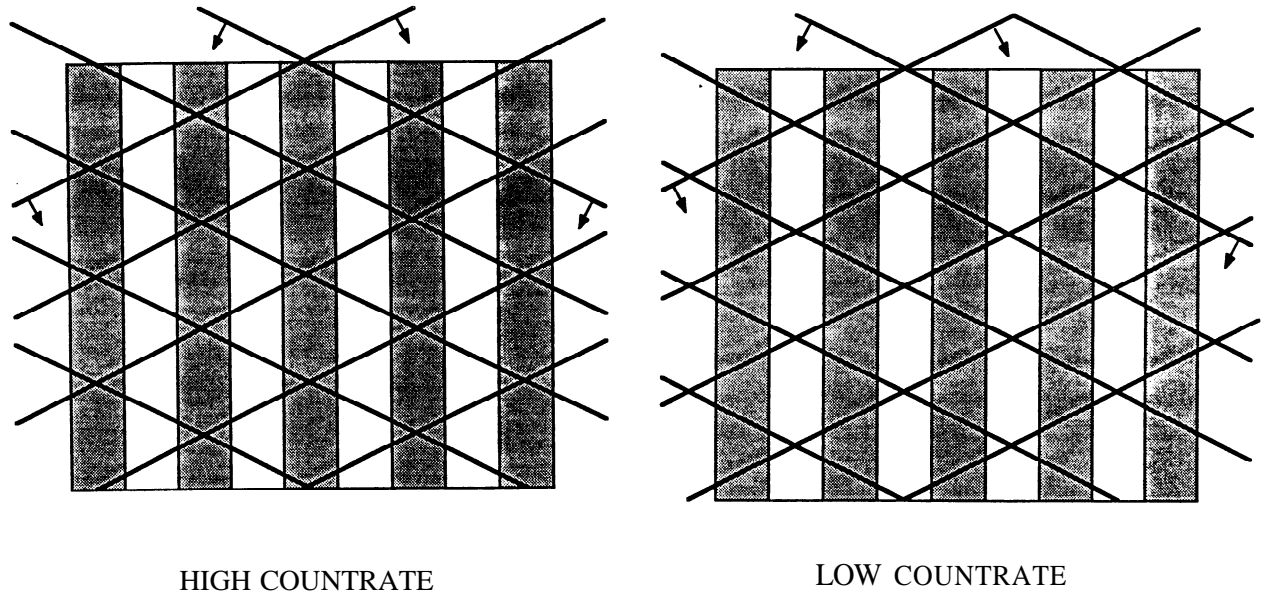


Figure 8: Operating principle of spatial heterodyne x-ray detector. Lines show the standing wave pattern produced in the detector by the interference of the subaperture pair. Bold lines are antinodes, and dashed lines are nodes. Light and dark shaded regions are layers of low and high efficiency in the laminar detector. Left panel shows phase of maximum countrate, and right panel shows minimum.

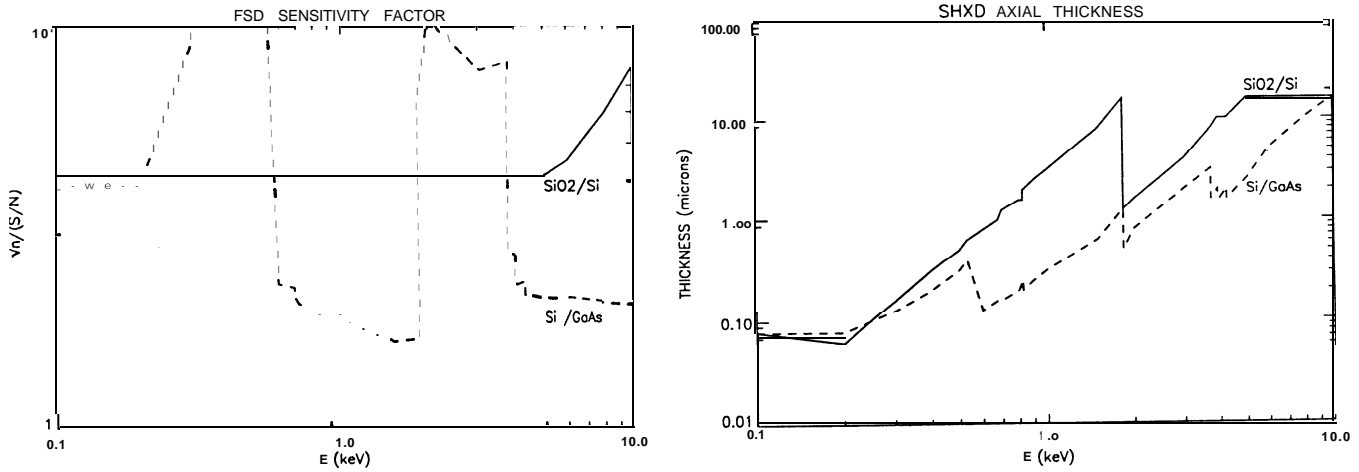


Figure 9: LEFT: Noise figure for spatial heterodyne detectors of Si/SiO₂ and Si/GaAs vs. x-ray energy. Required number of photons incident on the spatial heterodyne x-ray detectors can be calculated by multiplying the square of the above by $(S/N)^2$. RIGHT: Axial thickness of detectors vs. energy.

has been graphed as a function of energy in Figure 9 for an absorption spatial heterodyne detector consisting of a Si/SiO₂ and a Si/GaAs laminate. The axial thickness is chosen to be the optimal for each energy. The Si/SiO₂ detector has a very flat response over most of the band with $\sqrt{n_0}\sigma_V = 4$. For this, a visibility measurement with an error of $\sigma_V = 0.03$ would require 17800 photons to reach

the detector for a given point of the (u, v) -plane.

Note that spatial resolution is required in the dispersion direction to calculate the wavelength and (u, v) -plane coordinate associated with each detected photon. However, a resolution of $10\text{ }\mu\text{m}$ is more than adequate for this purpose. Higher resolution, which might be used to obtain the full spectral resolution delivered by the gratings, could be obtained by using large numbers of small fano-limited CCD pixels to centroid an event to $0.1\text{ }\mu\text{m}$.

Detector background is not likely to limit the interferometer. For a single subaperture pair and spectral order, a 30 m focal length, a grating with $1/d = 500\text{ l/mm}$, and $\lambda_{max} = 5\text{ nm}$, the active detector area is $15\text{ }\mu\text{m}$ by 8 cm (for $\Delta p = 100\text{ m}''$ and $\Delta q = 1\text{ m}''$). Roughly $8000(B/2.4m)(0.15\text{ nm}/\lambda)$ fringes would be produced and an equal number detector layer pairs required. The total area under one detector is 0.01 cm^2 . The observatory discussed below uses 288 such spectra and detectors, yielding a total area of 3 cm^2 . Since a typical source produces several million counts in 10^6 seconds (see below), the observations are background limited only if the background rate exceeds $B \sim 1\text{ ct/s/cm}^2$. This is two hundred times higher than the estimated background for the AXAF CCD, $B \sim 0.005\text{ ct/s/cm}^2$ (Garmire et al. 1986). If the underlying detector has energy resolution, even greater background rejection could be obtained.

The modulation produced by a spatial heterodyne detector is analogous to the Bormann effect in x-ray crystal diffraction, and to the use of Ronchi gratings. The Bormann effect is used by Bonse and Hart (1965) in their crystal x-ray interferometer. It should also be noted that the spatial heterodyne detector is in fact a grating. Half of the light diffracted into first order from one beam is diffracted into the direction and phase of the other beam. The remaining first order is diffracted into roughly twice the angle, giving fringes with half the period and therefore no modulation in the detector. The amount of light diffracted cannot exceed 5%, but is likely to be less.

Fabrication of a spatial heterodyne is a significant challenge, but within the reach of state of the art nanofabrication technology. Several plausible fabrication methods exist, including vacuum evaporation, sputtering, molecular beam epitaxy (MBE), metal-organic chemical vapor deposition, hydride vapor transport, hot wall epitaxy, and x-ray and e-beam lithography. The past decade has seen an explosion of developments in soft x-ray multilayer mirrors and in quantum superlattice structures. Both of these require ultra-precise laminar structures with spacings $< 3\text{ nm}$ and interfaces roughness $0.2\text{--}0.5\text{ nm}$ (rms). Multilayer mirrors have been constructed with layer thicknesses as small as 1 nm , using vapor deposition, sputtering and MBE. Typical layer pairs include ReW/C, W/C, NiC, Mo/Si, Si/SiO₂, and Si₃N₄. Quantum superlattices have been fabricated using MBE with alternating layers of AlAs and GaAs of minimum thickness 2.5 nm per layer (e.g. Leys et al. 1985). A wide variety of other superlattice combinations have been fabricated (cf. Weisbuch and Vinter 1991). Evaluation of these structures by x-ray diffraction and electron microscopy has proven that these techniques can achieve accuracies approaching tenths of nanometers. The effect of layer spacing accuracy and roughness can be estimated using equation (1). Assuming a Gaussian distribution of layer errors with $\sigma = 0.2\text{ nm}$, the largest B/X detector, with period $\Delta x = 2\text{ nm}$, would have its “visibility” reduced by only 5%. Equally important is the maintenance of precise lattice spacing over a large number of layers. This requires real time characterization and error compensation of the laminate during fabrication, a well developed approach in microfabrication technology.

E. Effective Area, uv-Coverage, and Sensitivity

Many subaperture pairs must be combined to obtain adequate sensitivity to most x-ray sources. Multiple subapertures can be accommodated in a single mirror shell, and a number of similar

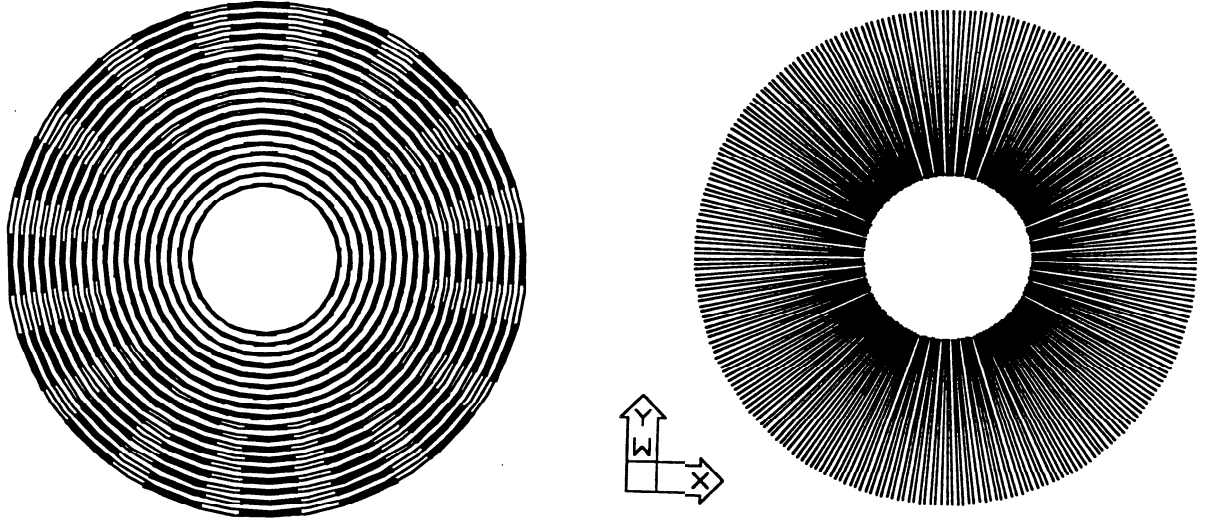


Figure 10 LEFT: X-ray interferometer subaperture pair layout, assuming 18 mirror shells and 8 pairs/shell. RIGHT: Resulting fringe spectra on focal plane detector; each line represents an entire fringe spectrum.

shells can be combined to build up adequate geometric area. The radial spectra from all subapertures can be detected on the same focal plane if the subaperture baselines all differ by more than $\Delta qd / (2\pi\lambda_{min}) \sim 0.1^\circ$ in azimuth. Thus more than 1000 baselines could in principle be focused onto the focal plane region. *Detection of all baselines on a single detector substrate is a critical feature of this design, as it makes possible the measurement of relative phases between different points in the (u, u) -plane.* Detection of visibility phases makes true imaging possible.

Each subaperture is assumed to be the rectangle inscribed in the mirror annular aperture that has the largest possible area. Then the aperture width is $\Delta\xi = C_1(\alpha)R_2$, and the length $\Delta\eta = C_2(\alpha)R_2$. The functions C_1 and C_2 depend on the parameter $\alpha = \gamma L / R_2$. The mirror outer radius is R_2 , and the length (of the paraboloid) is L . For AXAF, $\alpha = 0.02$, $C_1 = 0.014$, and $C_2 = 0.24$, which gives the area of each subaperture $a = 0.0033R_2^2$. Each pair uses a fraction $2C_2/\pi = 0.075$ of the circumference. With eight pairs, 40% of the mirror area is left over for other purposes (cf. III.G). The geometric area for interferometry can now be calculated from:

$$A_{geo} = 4C_1C_2N_{pair}R_{out}^2 f(n_{sh}, R_{in}/R_{out}). \quad (16)$$

For an outer radius $R_{out} = 2.4$ m, an inner radius $R_{in} = 0.6$ m, and **18** mirror shells spaced in diameter by 0.1 m, $f = 8.4$, and $A_{geo} = 6400$ cm². The aperture layout for this design is shown in Figure 10, along with the distribution of fringe spectra on the focal plane.

The broad-band response of this x-ray interferometer is a significant departure from most interferometric telescope designs. There are several important consequences. First, the (u, v) -plane coverage has some dependence on the source spectrum. For a line source the (u, v) -plane is sampled essentially discretely. However, for a continuum source, the (u, v) -plane is sampled continuously. To form an image from a two-dimensional array of visibility measurements, the continuum must be binned to a degree that depends on the number of counts and desired signal-to-noise ratio. If the actual source distribution is $S(\alpha, S)$, the Fourier transform of a binned visibility function with bin sizes Δu and Δv is

$$S'(\alpha, \delta) = \text{sinc}(\alpha\Delta u)\text{sinc}(\delta\Delta v)S(\alpha, \delta). \quad (17)$$

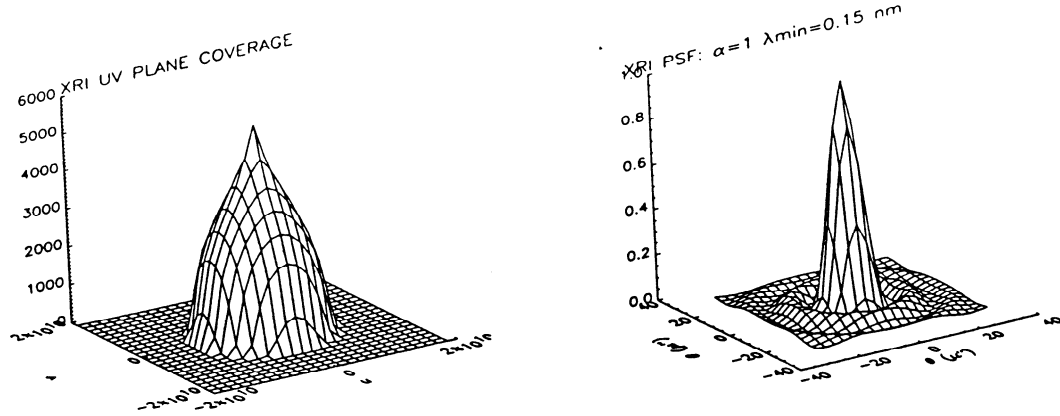


Figure 11: (u, v) -plane weighting function $W(u, v)$ and resulting point spread function, assuming a source with energy index $\alpha = 0.5$.

Binning in the (u, v) -plane by Δu effectively limits the field of view in image space to $1/\Delta u$. Sources larger than this must be observed multiple times with different phase tracking centers.

We can calculate the coverage of the (u, v) -plane by defining a weighting function $W(u)$ which gives the variation in the countrate as a function of the radial coordinate in the (u, v) -plane. This is calculated from $W(u) = \int C u^3 \lambda^2 p_\lambda \epsilon_\lambda d\lambda$, where the integral extends over wavelengths that contribute to that value of u , and p_λ is the source spectrum. We assume a power-law source $dF/dE \sim E^{-\alpha}$, and a wavelength independent efficiency, since the range of baselines will smear out most variations. The resulting function has the form

$$W(u) = C u^{(1-\alpha)} g(u, B_{max}, B_{min}, \lambda_{max}, \lambda_{min}) \quad (18a)$$

where the function g depends on the range of u :

$$g = (B_{max})^{\alpha+2} - (\lambda_{min} u)^{\alpha+2} \quad [u < B_{max}/\lambda_{max}] \quad (18b)$$

$$g = (B_{max})^{\alpha+2} - (B_{min})^{\alpha+2} \quad [B_{max}/\lambda_{max} < u < B_{min}/\lambda_{min}] \quad (18c)$$

$$g = (\lambda_{max} u)^{\alpha+2} - (B_{max})^{\alpha+2} \quad [u > B_{min}/\lambda_{min}] \quad (18d)$$

This weighting function $W(u)$ is illustrated in Figure 11 for a continuum source with $\alpha = 1$. Most AGNs have $0.5 < \alpha < 1.0$. The resulting point spread function is also shown. The psf changes very little when $\alpha = 0.5$. The psf has a FWHM of $12 \mu''$.

Using the above results, we can calculate the amount of time necessary to image various sources. In order to obtain an image with 200 (u, v) -plane bins (and an image with ~ 200 pixels), and signal-to-noise of 30 in each, an observation of 3C273 requires a 1.4×10^5 s (1.6 days). A source with 10% of the flux of 3C273 could be imaged in two weeks. Significantly less time would be required to obtain diameters, ellipticities, position angles, and existence of multiple emission regions.

We assumed above that the intensity distribution is independent of wavelength. Because of the very broad band of this interferometer, this will not be true for some objects. For example, AGN's

may contain a compact hard x-ray continuum source plus an extended soft x-ray emitting accretion disk. Binning can be performed in wavelength, with corresponding reduction in the dynamic range of the point spread function, and decreased signal to noise. Simple physical arguments suggest that in most cases source regions producing longer wavelength light will be more extended. These low energy components should be mapped with less angular resolution and a larger field of view. The detailed implications for various classes of object should be explored with simulations.

Time variability also leads to some difficulties. Low luminosity AGN's can have variability on minute to hour timescales. Stars with active coronae are generally rotating with periods of less than a week. For stars, the variation is predictable and therefore correctable. This is made possible by the simultaneous collection of all baselines of the u -plane image. In AGNs, some time averaging is inevitable. However, simple parameters such as the centroid of hard x-ray continuum emission can be measured very quickly, and tracked with time.

F. Mirror Figure, Phasing and Tracking

Maintaining phase control and phase knowledge is the foundation for any interferometer. For an x-ray interferometer, a phase knowledge of $2\pi/10$ radians requires path length measurements to fractions of an Angstrom. There are two goals: maintaining high fringe visibility, and determination of fringe phase.

Visibility is affected by the wavefront errors introduced in the optics, and by the optical path length difference between the two interfering beams. Path length differences must be less than a coherence length, which for the above design is $300 \mu\text{m} \lambda(nm)^2$. One of the key features of this design is this relaxed tolerance on the mean optical path difference.

A critical requirement of this concept is producing and maintaining grazing-incidence mirrors with surface quality exceeding by 40 times that of AXAF, and with five times the surface area! One key to doing this may be adapting the technique of active optics to x-ray mirrors. This is especially appropriate since the dominate contribution to fringe visibility loss is low spatial frequency errors. Also, in-orbit thermal gradients and material creep will result in long wavelength errors. Ceramic capacitor deformable Si mirrors now achieve a wavefront accuracy in the lab of 1-2Å rms with appropriate wavefront measurement systems. With an actuator spacing of 10 cm, the low frequency errors could be reduced by a factor of ~ 30 . Relaxed tolerance on low spatial frequency errors would ease the reduction of mid- and high-spatial frequency error during polishing. In orbit figure changes will have spatial period largely > 50 cm. Alternatively, a deformable mirror set could be used in the converging beam of the X-ray telescope, since the field of view of the instrument would be very small and therefore there would be no concern about pupil walk.

A metrology system must be incorporated in the telescope in order to measure the figure errors in orbit, or starlight must be used. A schematic of a Twyman-Green interferometer used for this purpose is sketched in Figure 12 (A Fizeau interferometer could also be used). One arm consists of a focussed beam which passes through the detector center and illuminates the entire x-ray mirror with coherent light. Mirrors mounted on the aperture plate, spaced at ~ 10 cm, and covering $\sim 10\%$ of the open aperture reflect the light back to the mirror and thence the interferometer. The second arm of the interferometer is a reference flat which can be translated parallel to the beam. The reference beam and the mirror beam interfere and are detected by the two-dimensional detector D . A two-dimensional map of path length errors in the system is obtained by scanning the reference flat through one wavelength and measuring the phase of the sinusoidal intensity modulation at each point on the detector D . The phase is obtained from the ratio of the first terms of the sine and cosine Fourier transform of the intensity modulation at each point (Bruning 1978). The required precision

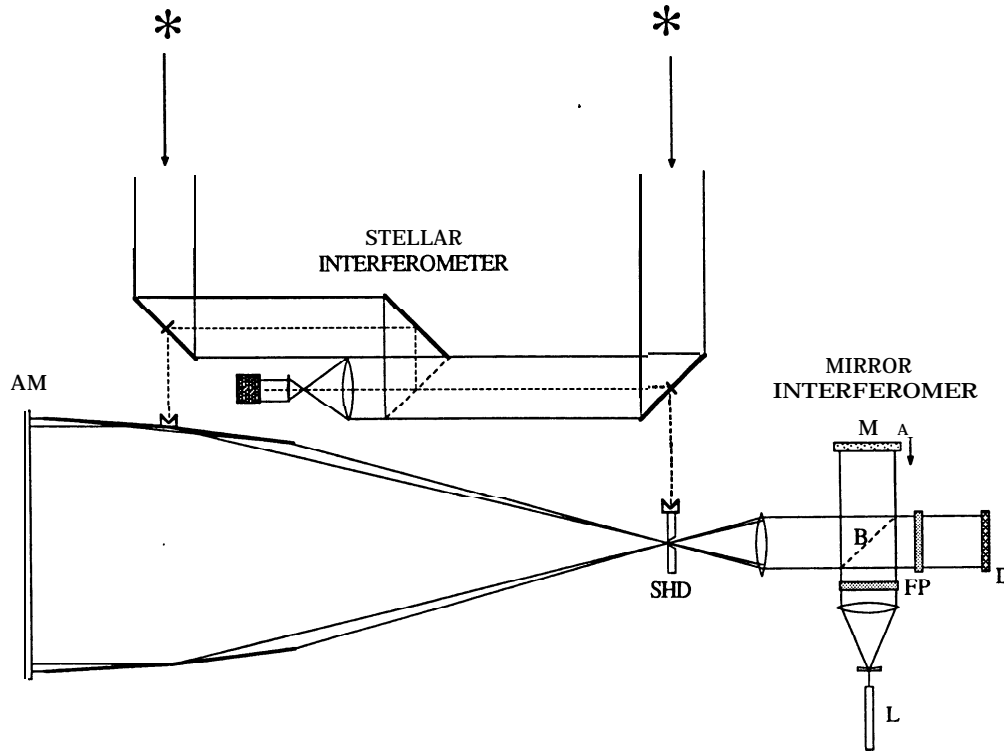


Figure 12: Metrology interferometer for determining mirror figure corrections and fringe phase. One of two stellar interferometers for obtaining inertial phase reference is also shown. Included in schematic are beam splitters (B), reference mirrors (M), Fabry-Perot mirrors (FP), metrology fringe phase detector (D), and x-ray detector (SHXD). Dotted lines are metrology links between mirror and stellar interferometer.

is $\Delta\phi \simeq \pi/10\lambda_X/\lambda_V \simeq 10^{-4}$. The accuracy of the phase measurement is limited by systematics (e.g. drifts, translation precision, beam walk and polarization leakage), since the photon-limited noise for a 5 mW laser would give a phase precision of $\Delta\phi \sim 10^{-6}$ rad in 0.1 s. This corresponds to $\lambda_V/60,000$. If systematics limit the precision for a single reflection Twyman-Green interferometer, multiple reflections can be used by interposing Fabry-Perot mirrors (FP) prior to the beam splitter. With a finesse of 60, the fringe phase would need to be measured to 0.006 rad or $\lambda_V/10^3$.

The fringe phase relative to the spatial heterodyne detector phase will be offset by several motions. All must be measured (but not controlled) to a small fraction of a fringe spacing so that the fringe modulation is not washed out. Table 1 summarizes the effects of various motions, the required accuracy of measurement, and the method of measurement. Two Michelson stellar interferometers (SI) with ~ 20 meter baselines along the x-ray telescope axis are pointed at bright stars and used to define an axis in inertial space. With 0.5 m mirrors, and observing 5^m stars, each interferometer will determine the component of the axis perpendicular to its baseline with a photon-limited accuracy

$$\Delta\theta \simeq 3 \times 10^{-11} [\Delta\lambda T]^{-1/2} 10^{-0.2(m_V-5)} [\text{rad}]. \quad (19)$$

where $\Delta\lambda$ is the visible interferometer bandwidth and T is the integration time. With $\Delta\lambda = 100\text{\AA}$, accuracy of $\Delta\theta = 10^{-11}$ would be obtained every 100 msec.

The mirror/detector phase center offset ($\Delta\mathbf{r}_{MD}$) and aperture/detector rotation angle ($\Delta\theta_{AD}$) are referenced to this stellar inertial axis interferometrically. The measured instantaneous phase offset

Table 1
X-Ray Interferometer Metrology Summary

Motion	Symbol	Affects	Measurement Tolerance	Measurement Method	Control Tolerance
Mirror/Detector Phase	$\Delta \mathbf{x}_{MD}$	$\Delta \phi$	0.1 nm	Stellar IF	1 μm
Mirror/Detector Axial	Δz_{MD}	V	1 μm	Mirror IF	1 μm
Mirror Tilt	$\Delta \alpha_M$	$V, (\text{coma}) \Delta \phi$	100 m''	Mirror IF	100 m''
Detector/Aperture Rotation	$\Delta \theta_{AD}$	$\Delta \phi$	10 m''	Stellar IF	1''
Detector Tilt	$\Delta \alpha_D$	V	2''		2''
Aperture Translation	$\Delta \mathbf{x}_A$	small			
Aperture Scale	M_A	ΔB	10^{-5}		Material
Mirror Figure	$\Delta \xi, \eta$	$V, \Delta \phi$	0.3 nm (rms)	Mirror IF	0.6 nm

$\Delta \phi$ is then associated with detected photons of wavelength λ , where

$$\Delta \phi = \frac{k}{F} \mathbf{B} \Delta \mathbf{x}_{MD} + \frac{2\pi}{d} \mathbf{B} \times \Delta \theta_{AD} + \Delta \phi_{MF}(\lambda, \mathbf{B}). \quad (20)$$

Phase offsets can also be introduced intentionally by translating or rotating the detector. Periodic observation of a bright “point source” of x-rays, such as Sco X-1, would be used to recalibrate the optical/x-ray metrology link. For example, Sco X-1 would produce a countrate of $\sim 10^5$ ct/s. In one hour, this would provide calibrations accurate to 1% over 10^3 baselines.

While the pointing direction must be tracked very accurately, the pointing control requirement is much less severe. It is limited in two ways: the off-axis aberrations of the telescope/grating combination, and the physical size of the spatial heterodyne detectors. An estimate of the effect of off-axis aberrations yields a limit of ~ 1 arcsecond on the pointing error. The detector size is likely to be in the range of 0.1- 1 arcsecond (in the baseline direction), but this depends on the detector technology employed. More precise limits will require further analysis and detector development. This pointing control requirement is within the capability of observatory-class spacecraft.

G. Low Resolution Channel

The x-ray interferometer spans an angular range of $10 \mu'' < \theta < 1 m''$. In order to obtain lower resolution angular information, the 30% remaining aperture is devoted to a low resolution spectroscopic imaging channel. The interferometer apertures are chosen so that the leftover apertures coincide at 16 azimuthal positions. The beams from these sectors are diverted to different detectors using reflection or transmission gratings with rulings orthogonal to those of the interferometer gratings. The resulting line spectra contain imaging information with 1 m'' resolution perpendicular to the dispersion direction (e.g. Cash 1990), and $\Delta \lambda / \lambda \sim 10^3$. the one-dimensional information obtained at eight or more position angles can be combined and deconvolved to produce a two-dimensional spectrally resolved image. These lower resolution data are also necessary to determine the pointing direction and phase center for the interferometric observations.

H. Ground-Based Testing and Calibration

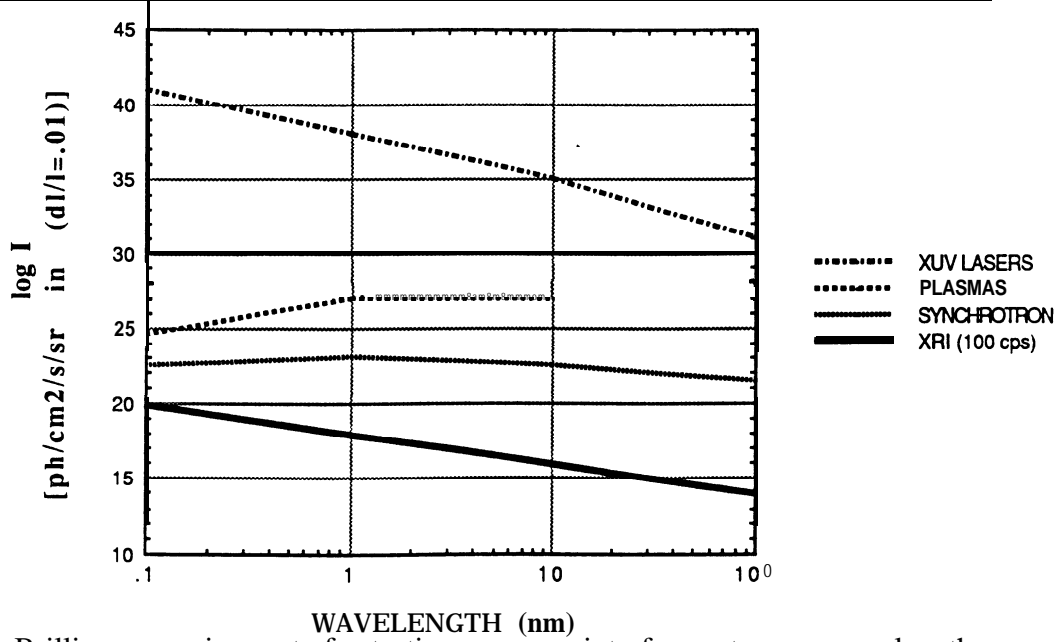


Figure 13: Brilliance requirements for testing an x-ray interferometer, vs. wavelength, compared to the performance of various x-ray sources.

As the old saying goes, “if you can’t test it, you can’t build it”. In this section we consider plausible test setups for the proposed interferometer. Each baseline (subaperture pair) of the interferometer operating at a wavelength λ has an area-solid angle product $A\Omega = C_1 \lambda^2 \epsilon$, where C_1 was defined in III.E, and ϵ is the system efficiency. Testing can be performed by illuminating the interferometer with a diffracting slit placed at some distance away. The slit width and height appropriate for the angular resolution of the interferometer is the same as that required to place both mirror sections within its Fresnel zone. The dependence on λ leads to more stringent requirements for source intensity at short wavelengths. The requirements and performance of various sources are illustrated in Figure 13. Electron impact and gas discharge sources produce weak countrates, barely adequate for testing. It may be possible to enhance the efficiency of electron impact sources by constructing a spatially modulated emission region which would be used directly as the test object instead of the diffracting slit. A synchrotron source followed by a diffracting slit is more than adequate. In both cases, a long tube ($\sim 10^3$ km) would be required between the source and the interferometer, in order to minimize aberrations introduced by finite conjugates.

I. Simulations and Potential Targets

Capella. X-ray interferometric observations of Capella would yield images of its stellar corona with a resolution of $<5\%$ of the disk diameter. A simulation of the quality of data that could be obtained is shown in Figure 14. A soft x-ray image of the sun, obtained by Skylab, has been used as a model of the Capella corona. A (u, v) -plane image transform with ~ 600 baselines of $S/N=30$ could be obtained in 10^5 s (one day at 100% efficiency). Using the spectroscopic capability of this mission, several days of observing would provide images of the corona at different temperatures. The time-evolution of the coronal structures could be studied over longer periods. This data would give unparalleled information about coronal heating, stellar magnetism, the stellar dynamo, stellar structure and evolution. A number of other x-ray bright stars are also excellent candidates for study, including OB supergiants, T Tauri stars, and RS CVn stars. A selection of these are listed in Table 2.

NGC 4151. NGC4151 is believed to consist of a central nonthermal source of size $<10^{15}$ cm, surrounded by x-ray absorbing broad-line region clouds of dimension $\leq 10^{14}$ cm which-cover 90%

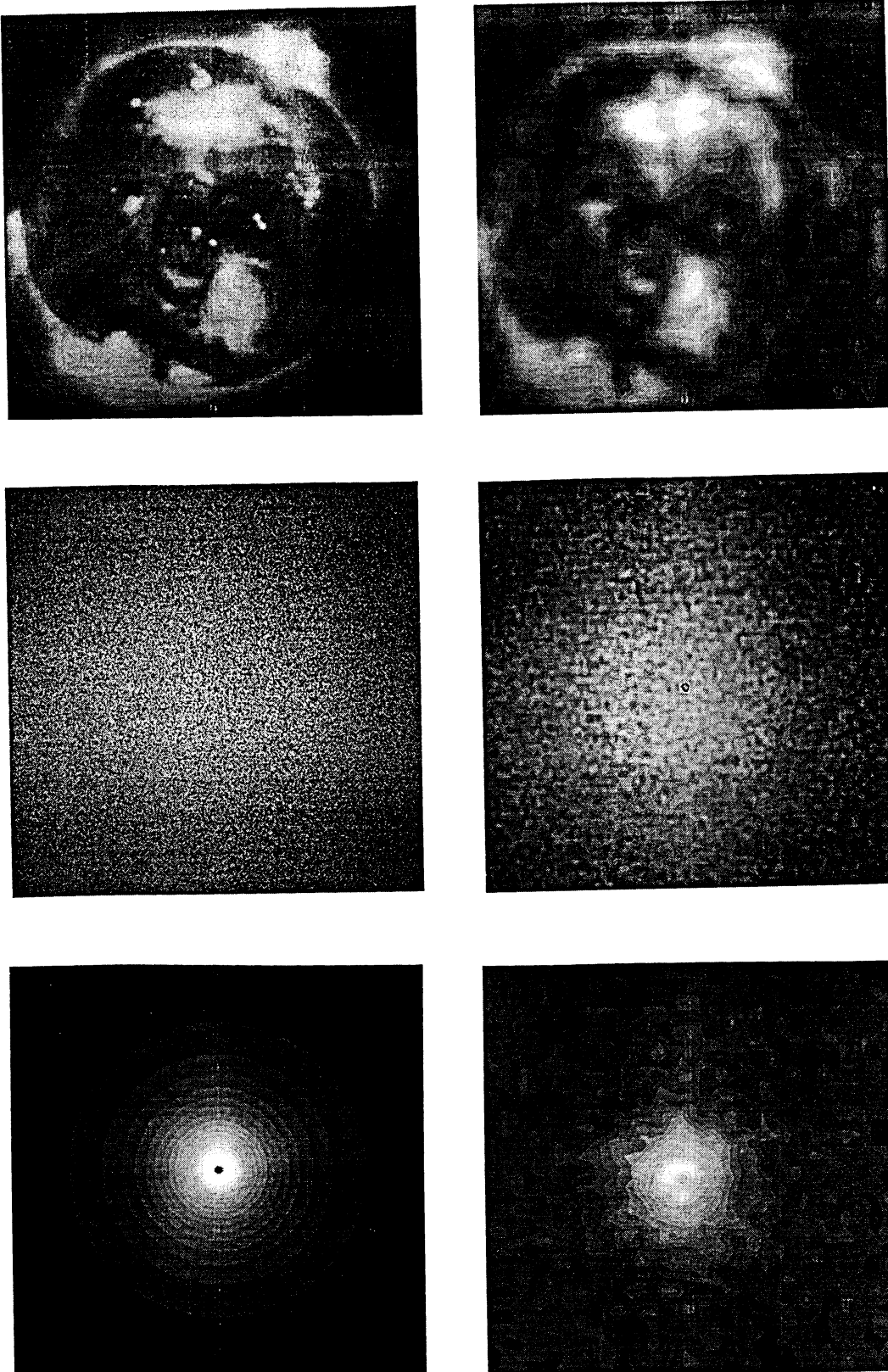


Figure 14: Simulations of imaging with x-ray interferometric observatory. TOP: “Capella” MID-DLE: NGC 415 1. Bottom: 3C273. LEFT: source; RIGHT: derived image.

Table 2
A Sample of X-ray Interferometry Targets

OBJECT	TYPE	log D(cm)	F_x	log F_{FeK}	log ΔR (cm)	Light Time/ # Pixels ¹	Tint (10 ⁵ s)
3C273	QSO	27.3	6	-4.3	16.8	22 lt-days	1.5
NGC 5548	Sy I	26.3	0.5	-4.2	16.1	5 lt-days	30
NGC 4151	Sy I	25.6	10	-3.5	15.0	8 lt-hrs	1.0
Cen A	AGN	25.7	20	-4.0	15.6	33 lt-hrs	0.5
NGC 7469	AGN	26.3	0.8	-4.2	16.2	6 lt-days	11
IC 4329A	AGN	26.3	2.2	-3.8	16.2	6 lt-days	4.1
MGC 6-30-15	AGN	25.6	2.0	-4.1	15.5	30 lt-hrs 4.5	
NGC 3227	AGN	25.6	0.8	-4.3	15.5	30 lt-hrs	11
NGC 6814	AGN	25.8	7	4.4/-3.6	15.7	36 lt-hrs	1.3
1E1821+64	QSO	27.6	1.8		17.3	77 lt-days	5
PKS2155-304	BL Lac	27.1	27		16.9 5	24 lt-days	0.3
F9	AGN	25.7	160		15.5	30 lt-hrs	0.06
M87	AGN	25.9	52		15.7	36 lt-hrs	0.2
NGC 1275	AGN	26.5	29		16.3	7 lt-days	0.2
M82	AGN	25.1	6		14.9	7 lt-hrs	1.5
SN 1980k	SNe	25.5			15.78	4	
Her X-1	XR pulsar	22.2	160		12.0	30 lt-set	0.06
cyg x-1	BH binary	21.9	500		11.7	15 lt-sec	0.02
Sco X-1	LMXRB	21.3	10,000		11.1	4 lt-sec	0.00 1
ss 433	Binary	22.2	10		12.0	30 lt-sec	0.9
ζ Pup	04f	21.1	5		11.4	12	1.8
ϵ Ori	B0Ia	21.1	2.7		11.4	23	3.3
κ Ori	B0.5Ia	21.2	0.8		11.5	20	11
β Per	B star	20.0	6		10.3	50	1.5
Capella	F9III	19.6	30		9.9	23	0.3
α Tri	F star	19.8	3.0		10.1	20	3.0
a Cen A	G2	18.8	1.3		9.1	160	7.0
24 UMa	G star	19.9	6		10.2	12	1.5
70 Oph B	K star	19.2	4.0		9.5	50	2.3
EQ Vir	K star	19.8	2.2		10.1	12	4.1
ϵ Eri	K2V	19.0	2		9.3	70	4.5
α Cen B	K5	18.8	2.7		9.1	125	3.3
UV Cet	FS (M6)	18.9	7		9.2	33	1.3
WOLF 630	M star	19.3	6		9.5	15	1.5
EQ Peg AB	M star	19.3	5		9.6	15	1.8
Prox Cen	M star	18.6	4.5		8.9	250	2.0
Sirius B	DAWD	18.9	1		9.2	~1	9.0
DG Tau	T Tauri	20.7	2		>11	>6	4.5
HR1099	RS CVn	20.0	18		10.3	68	0.5
AR Lac	RS CVn	20.1	8		10.4	33	1.1
UX Ari	RS CVn	20.2	7		10.5	60	1.3

¹ Resolution of x-ray interferometer expressed in light-seconds or in number of pixels over a stellar disk (in one dimension).

of the central x-ray source at any given time (Holt *et al.* 1980). In addition, these cold clouds may be in pressure equilibrium with a hot intercloud medium of dimensions 10^{17} cm, also largely obscured by the BLR clouds. In Figure 14, I show an x-ray interferometry simulation that assumes the hot intercloud gas accounts for 20% of the total emission from the AGN. This observation required 3×10^5 s (3 days) and uses 450 baselines. The fluctuations that appear in both images are produced by broad-line cloud absorption. With this data, it will be possible to determine whether there is a hot intercloud medium in the BLR, begin to study the statistics of the BLR absorbing clouds and determine whether they are in a random, spherical distribution or a more organized, “disk-like” grouping, and to locate the Fe K fluorescence (e.g. BLR or accretion disk).

3C273. In 3C273 and several other bright QSOs and AGNs, it may be possible to use Fe K and L shell fluorescence to demonstrate the existence of an accretion disk and begin to map out its structure. Considerable evidence has accumulated that Fe K fluorescence features in AGN are produced by the fluorescent reflection of a nonthermal x-ray source from cold matter with a large solid angle. Some have speculated that this is a signature of the accretion disk feeding a supermassive black hole. Using the combination of imaging and spectroscopy that this observatory would provide, it would be possible to obtain a spatially resolved spectrum of the reflected emission. This data would prove the existence of an accretion disk, begin to map its structure, and yield a definitive mass determination for the central object. In addition, depending on the mass of the central black hole, it may be possible to crudely resolve the inner accretion disk and the nonthermal continuum source. Figure 14 shows the results of a simulation assuming 10^6 of integration time and 450 baselines with $S/N=50$ per baseline. Table 2 gives a selection of other AGNs with bright fluorescent Fe lines.

J. Beyond Fizeau to Michelson

It is interesting to realize that the interferometer presented in this paper, were it ever to be constructed, would provide a natural starting point for future efforts. Fizeau’s original concept obtained diffraction limited resolution from a single telescope aperture. Michelson’s stellar interferometer could provide a much longer baseline with the same focal plane fringe spacing. An x-ray realization of Michelson’s stellar interferometer is sketched in Figure 15, which uses the Fizeau x-ray interferometer as a beam combiner and fringe detector. Clearly, such an instrument would require technology far beyond the state of the art. The development of the broadband Fizeau x-ray interferometer presented in this paper will lead to exhilarating insights into the universe. It is exciting to think that it would also lay the foundation for a long baseline x-ray interferometer that will map the magnetospheres and surfaces of neutron stars, explore the structure of accretion disks in binaries, and survey the event horizons of black holes with sub-Schwarzschild radius resolution.

IV. Summary and Development Issues

I have presented a concept and preliminary design for an x-ray interferometric observatory that obtains a spectral resolution of $E/\Delta E > 10$ and true imaging with angular resolution of $10 \mu''$. The observatory operates over a broad band (0.2-8 keV) and delivers spectrally resolved images of a variety of x-ray sources. Phase stability is made straightforward by using monolithic mirrors and detectors, and is maintained using laser metrology. The concept exploits many techniques currently under development for the Astrometric Interferometry Mission (AIM), under consideration for a new start near the turn of the century. This angular resolution, 10^5 times better than AXAF, is necessary to obtain a detailed understanding of the geometry and physical conditions in a variety of x-ray sources. Observations with this facility will lead to fundamental new insights into the origin, structure and evolution of stars and stellar magnetism, x-ray binaries, accretion disks, black holes,

Michelson X-ray Stellar Interferometer

Baseline extension array module + Broad-Band X-ray interferometer

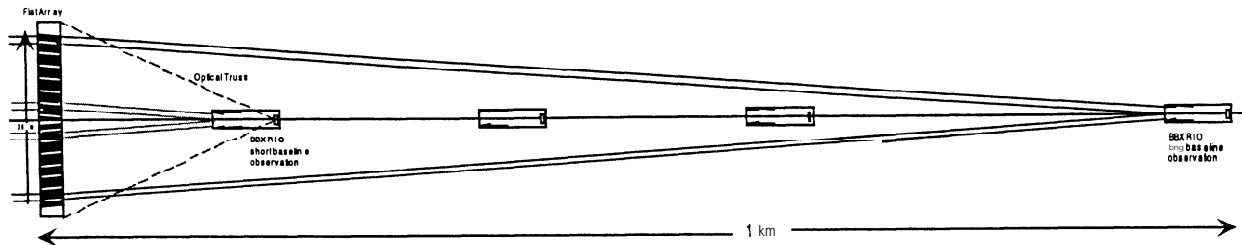


Figure 15: An x-ray realization of Michelson's stellar interferometer. The broadband Fizeau x-ray interferometer acts as beam combiner and fringe detector. Long baselines are obtained with grazing incidence folding flats. The folding flat array and BBXRI are operated as separated spacecraft, with optical trusses supplying alignment knowledge, and TBD control systems.

active galactic nuclei and quasi-stellar objects.

To make this observatory possible, several areas of development must be pursued. Five are particularly relevant to this instrument: (1) improvements in grazing-incidence mirror fabrication techniques; (2) development of spatial heterodyne x-ray detectors; (3) investigation of the potential of active x-ray optics; (4) investigation of the practical limits of optical interferometric metrology; and (5) development of space-based platforms for interferometry. Elements (4) and (5) are under active investigation for the Astrometric Interferometry Mission (AIM), a NASA optical-UV interferometry mission planned for a new start around 1999. Improvements in mirror fabrication techniques will be a direct byproduct of the AXAF development. New efforts must be initiated to explore the possibility of active x-ray optics and spatial heterodyne x-ray detectors.

References

- Becker, P., Seyfried, P., and Siegert, H. 1987, *Rev. Sci. Instrum.*, **58**, 207.
- Bonse, U., and Hart, M. 1965, *Appl. Phys. Lett.*, **6**, 155.
- Born, M., and Wolf, E. 1980, *Principles of Optics*, Pergamon Press, Oxford.
- Bresse, J. 1972, in *Scanning Electron Microscopy*, 5th Annual Symposium, Chicago.
- Bruning, J. H. 1978, in *Optical Shop Testing*, Wiley & Sons, New York.
- Cash, W. C., Jr. 1983, *Appl. Opt.*, **22**, 3971.
- Cash, W. 1990, in *Proceedings of the Workshop on High-Energy Astrophysics in the*

21st Century, in press.

Deslattes, R. D., and Henins, A. 1973, *Phys. Rev. Lett.*; 31,972.

Fizeau, C. R. 1868, *C. R. Acad. Sci. Paris*, 66, 934.

Hettrick, M. C., and Bowyer, S. 1983, *Appl. Opt.*, 22, 3921.

Holt, S.S., *et al.* .1980, *Ap.J.Lett.*, 241 L13.

Kellström, G. 1932., *Nova Acta Regiae Societatis Scientiarum Upsaliensis*, 8, No. 5.

Kulkarni, S.R. 1988, Proc.ESO Conf. No. 29, *High Resolution Imaging by Interferometry*, p. 595.

Lee, P. 1982, *Opt. Commun.*, 43, 237.

Leys, M. R., *et al.* 1985, *J. Cryst. Growth*, **68**, 43 1.

Martin, C. 1990, in *Astrophysics from the Moon*, AIP Conf. Proc. 207, ed. M.J. Mumma, H.J. Smith, p. 409.

Michelson, A. 1920, *Ap. J.*, 51,257.

Rocket, P. 1985, Proposal to the National Science Foundation.

Schroeder, D. 1987. *Astronomical Optics*, Academic Press, San Diego, pp. 258-27 1.

Shao, M., *et al.* 1988, *Astr. Ap.*, 193, 357.

Shealy, D.L., Hoover, R.B., Walker, A.B.C, and Barbee, T.W. 1989, in *X-ray/EUV Optics for Astronomy and Microscopy*, Proc. SPIE Vol. 1160, p. 94- 107.

Van Speybroeck, L., *et al.* 1989, in *X-ray/EUV Optics for Astronomy and Microscopy*, Proc. SPIE Vol. 1160, p. 94-107.

Weisbuch, C., and Vinter, B. 1991, *Quantum Semiconductor Structures*, Academic Press, San Diego.